



## Grain boundary mobilities in polycrystals

Zhang, Jin; Ludwig, Wolfgang; Zhang, Yubin; Sørensen, Hans Henrik B.; Rowenhorst, David J.; Yamanaka, Akinori; Voorhees, Peter W.; Poulsen, Henning F.

*Published in:*  
Acta Materialia

*Link to article, DOI:*  
[10.1016/j.actamat.2020.03.044](https://doi.org/10.1016/j.actamat.2020.03.044)

*Publication date:*  
2020

*Document Version*  
Publisher's PDF, also known as Version of record

[Link back to DTU Orbit](#)

*Citation (APA):*  
Zhang, J., Ludwig, W., Zhang, Y., Sørensen, H. H. B., Rowenhorst, D. J., Yamanaka, A., Voorhees, P. W., & Poulsen, H. F. (2020). Grain boundary mobilities in polycrystals. *Acta Materialia*, 191, 211-220. <https://doi.org/10.1016/j.actamat.2020.03.044>

---

### General rights

Copyright and moral rights for the publications made accessible in the public portal are retained by the authors and/or other copyright owners and it is a condition of accessing publications that users recognise and abide by the legal requirements associated with these rights.

- Users may download and print one copy of any publication from the public portal for the purpose of private study or research.
- You may not further distribute the material or use it for any profit-making activity or commercial gain
- You may freely distribute the URL identifying the publication in the public portal

If you believe that this document breaches copyright please contact us providing details, and we will remove access to the work immediately and investigate your claim.



Full length article

## Grain boundary mobilities in polycrystals

Jin Zhang<sup>a,b</sup>, Wolfgang Ludwig<sup>c</sup>, Yubin Zhang<sup>d</sup>, Hans Henrik B. Sørensen<sup>e</sup>,  
David J. Rowenhorst<sup>f</sup>, Akinori Yamanaka<sup>g</sup>, Peter W. Voorhees<sup>a</sup>, Henning F. Poulsen<sup>\*,b</sup>

<sup>a</sup> Department of Materials Science and Engineering, Northwestern University, Evanston, IL 60208, USA<sup>b</sup> Department of Physics, Technical University of Denmark, Kongens Lyngby, Denmark<sup>c</sup> European Synchrotron Radiation Facility, Grenoble, France<sup>d</sup> Department of Mechanical Engineering, Technical University of Denmark, Kongens Lyngby, Denmark<sup>e</sup> Department of Applied Mathematics and Computer Science, Technical University of Denmark, Kongens Lyngby, Denmark<sup>f</sup> Materials Science and Technology Division, The US Naval Research Laboratory, Washington, DC 20735, USA<sup>g</sup> Division of Advanced Mechanical Systems Engineering, Institute of Engineering, Tokyo University of Agriculture and Technology, Tokyo 184-8588, Japan

## ARTICLE INFO

## Article History:

Received 2 December 2019

Revised 19 February 2020

Accepted 25 March 2020

Available online 7 April 2020

## Keywords:

Phase field

Grain growth

Ferrite

Microstructure

X-ray synchrotron radiation

## ABSTRACT

Most metals, ceramics, semiconductors and rocks are composed of small crystals known as grains. When annealed, this polycrystalline structure coarsens, thus allowing the properties of a material to be tailored for a particular application. The mobility of grain boundaries is thought to be determined by the crystallography of the adjacent crystals, but experimental validation in bulk polycrystalline materials is lacking. Here we developed a novel fitting methodology by direct comparison of a time-resolved three-dimensional experimental data to simulations of the evolution of 1501 grains in iron. The comparison allows reduced mobilities of 1619 grain boundaries to be determined simultaneously. We find that the reduced mobilities vary by three orders of magnitude and in general exhibit no correlation with the boundary's five macroscopic degrees of freedom, implying that grain growth is governed by other factors.

© 2020 Acta Materialia Inc. Published by Elsevier Ltd. This is an open access article under the CC BY license.

[\(http://creativecommons.org/licenses/by/4.0/\)](http://creativecommons.org/licenses/by/4.0/)

## 1. Introduction

Most crystalline materials are composed of many small crystallites, grains, with lattices of different orientations. The boundaries between the grains can move to reduce the total grain boundary energy of the ensemble. Since many mechanical and physical properties of materials, from tensile strength in structural materials to resistivity in electronic materials, are a function of the local grain morphology, grain growth can be used to design materials with a given set of properties. The predictive power of models of this grain growth process is critically dependent on understanding the mechanisms governing the grain boundary movement and measurements of the relevant materials parameters.

The local velocity of a grain boundary is given by  $v = -m\kappa$ , where  $\kappa$  is the total curvature of the boundary and  $m$  is the reduced grain boundary mobility,  $m = M\gamma_o$ . Here  $M$  is the grain boundary mobility, and  $\gamma_o$  is the grain boundary stiffness (see Section S3.8 in supplementary materials). The reduced mobility measures the rate by which a boundary can move under the driving force of grain boundary energy. Analytical models of grain growth have exploited the similarity between the interfacial energy driving force for polycrystalline

grain growth and soap froth evolution [1–3]. However, these models neglect the anisotropic crystalline nature of grains and grain boundaries, and assume an isotropic growth where  $M$  and  $\gamma_o$  are constants.

The crystallography of a grain boundary can be described by five macroscopic degrees of freedom representing the misorientation (the orientation difference between the two grains that share the boundary) and the inclination of the grain boundary plane [4,5]. The grain boundary energy is a function of these five macroscopic degrees of freedom [6,7]. Measuring grain boundary velocities at the surface of bicrystals has led to the conjecture that the mobilities are likewise determined by these same five degrees of freedom [5,8,9]. However, only a limited number of mobilities can be determined in this way, and it is not clear if the measurements represent grain growth observed in three-dimensional polycrystalline materials.

The phase-field method has emerged as a powerful tool to simulate microstructure evolution [10,11]. It has been successfully applied to study grain growth [12–16]. The phase-field method can also incorporate the dependence of grain boundary mobility on the five macroscopic degrees of freedom [10,11,13–15,17]. However, these models have only been compared to experiments in an indirect statistical or qualitative way, due to the lack of experimentally measured grain boundary mobilities. It is possible to determine grain boundary mobilities using molecular dynamics simulations. For example, atomistic simulations of bicrystals indicate that the mobility can vary strongly with

\* Corresponding author.

E-mail address: [hfpo@fysik.dtu.dk](mailto:hfpo@fysik.dtu.dk) (H.F. Poulsen).

misorientation [18,19] and that a small fraction of low mobility boundaries in a sample can lead to grain growth stagnation [20]. However, there is no experimental validation; therefore, it would be interesting to determine if mobilities calculated using bicrystals can be applied to grain growth in polycrystals. In another approach, the mobility is represented by disconnections in the boundary [21–23] and thus the mobility may not be an intrinsic property of a grain boundary [24]. However, all the factors setting the disconnection content of a given grain boundary in an evolving polycrystal are unknown. Thus, measuring reduced grain boundary mobilities for a large number of boundaries in the interior of a polycrystal is essential in understanding the mechanisms controlling grain growth in the polycrystalline systems found in real-life materials.

During the last 15 years, nondestructive 3D grain mapping techniques based on the use of synchrotrons have been developed, such as three-dimensional x-ray diffraction (3DXRD) [25] and diffraction contrast tomography (DCT) [26,27], which provide a possible remedy to the problems. These techniques allow the study of grain growth within bulk polycrystalline samples. Schmidt et al. [28] firstly applied 3DXRD in studying grain growth of 480 Al-Mn grains with six time-steps and a spatial resolution of about 5–8  $\mu\text{m}$ . Researchers in Robert Suter's group have used 3DXRD to study grain growth in pure nickel [29] and pure iron [30] with slightly improved resolution but fewer time-steps. Syha [31] and Trenkle [32] used DCT to measure the growth of 849 grains in strontium titanate with two steps and a voxel size of 0.7  $\mu\text{m}$ . Sun et al. [33] used a laboratory-based DCT method [34,35] to measure three steps of grain growth of 300 iron grains with a voxel size of 5  $\mu\text{m}$ . However, in all cases, no reduced mobilities for individual grain boundaries have been reported.

In this work, we report on results extracted from time-resolved x-ray diffraction contrast tomography of grain growth in a polycrystalline iron sample. A novel fitting methodology developed previously by direct comparison between phase-field simulations and a coarsening experiment [36] is extended for measuring reduced grain boundary mobilities. By coupling 3D phase-field modeling with 3D grain growth experiments, we simultaneously fit the reduced mobilities for a large number of grain boundaries resulting in a rapid throughput technique for measuring grain boundary properties. In this paper, we focus on the fitting methodology and its application in measuring the reduced grain boundary mobilities in pure iron. The fitting results are analyzed within the classical framework of grain growth, *i.e.*, by investigating the correlation between the reduced grain boundary mobilities and the five macroscopic degrees of freedom. We find, using a bulk polycrystalline sample, that in general there is no correlation between the reduced grain boundary mobility and the five macroscopic degrees of freedom of grain boundaries and, moreover, that the reduced mobilities can vary with time. This is in contrast to the conventional understanding and implies that grain boundary motion in polycrystals is governed by factors other than simply the crystallography of the component crystals.

## 2. Methods

### 2.1. Experiment

The raw material is Armco iron with 99.9 wt% purity. The main impurities are Mn (0.074 wt%) and Ni (0.014 wt%). The raw material was cold-rolled to 50% reduction in thickness, and then annealed at 700°C for 30 min. Vickers hardness tests and light optical microscopy showed that the material had been fully recrystallized with an average grain size (equivalent grain radius) of 20  $\mu\text{m}$ . The crystallographic texture of the sample was close to random [37]. After the pre-annealing, the material was cut by wire electrical discharge machining into 1 mm diameter rods with the rolling direction along the cylinder axis. To remove the damage from cutting, the rods were further electrochemically etched to a diameter of 500  $\mu\text{m}$ .

The in-situ grain growth experiment was carried out at the materials science beamline ID11 at European Synchrotron Radiation Facility (ESRF). The beamline operates an end-station optimized for monochromatic beam 3D X-ray diffraction and tomographic imaging experiments. X-ray diffraction contrast tomography, DCT [26,27,38,39], is an extended beam, diffraction imaging approach enabling rapid volumetric mapping of grains and orientations within extended 3D sample volumes based on a single rotational scan (typically mapping 400<sup>3</sup> voxels in 1 h). The metallic sample adhered to a low thermal conductivity ceramic sample holder (2 mm Alumina tube) with a high-temperature glue. The sample holder was mounted on the tomographic rotation stage of the diffractometer which was rotated continuously over 360 degrees during x-ray exposure. The double-crystal Si (111) Laue–Laue monochromator was set to an energy of 40 keV and delivered a uniform beam with a relative bandwidth of  $1 \times 10^{-3}$ . A compound refractive lens [40] was used to collimate and condense the beam. The extent of the mapped sample volume was defined by a slit, placed in close proximity to the sample. The slit opening was 400  $\mu\text{m}$  vertically and 600  $\mu\text{m}$  horizontally. The transmitted and the diffracted beams were simultaneously recorded on a high-resolution near-field x-ray imaging detector with 2048  $\times$  2048 pixels and an effective pixel size of 1.54  $\mu\text{m}$ . The detector-to-sample distance was 4.65 mm, thereby enabling the recording of the first 5 hkl families of diffraction spots from individual grains. Each of the DCT scans comprised 3600 images, corresponding to rotation steps of 0.1 degrees, each with an exposure time of 1s.

The sample was alternately mapped in air at room temperature and annealed on the beamline with a retractable tube furnace operating at 800°C. Forming gas (Ar+2%H<sub>2</sub>) flowed through the tube furnace to prevent sample oxidation. After annealing, the sample was cooled by a jet of forming gas and allowed to stabilize for 5 min before starting a new DCT scan. In total 14 annealing steps (with annealing time of 5 min) and 15 DCT scans were performed at room temperature. The annealing time between the first and the second scan was not determined as accurately as the rest; thus, this first scan was not used in the fitting procedure. The data was analyzed using the DCT software package<sup>1</sup> following the procedures summarized in [26,39]. The orientations of all grains and the grain boundary positions were mapped with a resolution of 0.1 degrees and 1.5–3  $\mu\text{m}$ , respectively [37]. By inspection of the evolution of the reconstructed grain boundaries, we suspect that the spatial resolution of the relative boundary movement can be less than one voxel (see Figure S1). Details of the data analysis procedure are provided in Section S1 of supplementary materials.

The resulting 3D experimental data of grain growth is shown in the supplementary video 1. A statistical analysis of the evolution of the grain ensemble showed that the growth of the average grain size is somewhat consistent with classical isotropic grain growth models [3], while the growth rates of individual grains are not consistent with these models [37].

### 2.2. Phase-field method

Generally speaking, each grain is modeled by an implicit representation where a phase-field variable, has a value 1 inside the grain, 0 outside, and a smooth transition from 0 to 1 near the grain boundary. Anisotropy in grain boundary energies and grain boundary mobilities can be built in the model [14,15]. For simplicity, in the work presented here, the inclination dependence of the reduced grain boundary mobility does not vary along a boundary, but can vary from boundary to boundary, see supplementary materials (Section S3.8). Thus, the inclination dependence of the reduced grain boundary mobility can be examined by looking at boundaries with the same

<sup>1</sup> <https://sourceforge.net/projects/dct>

misorientation but different boundary inclinations. The model used is related to [15]. It is described in detail below.

Assume there are  $p$  grains in the system. Let grain  $\alpha$  be described by a phase-field variable  $u_\alpha$ . Then the evolution of each phase-field variable  $u_\alpha$  during grain growth is described by the vector-valued Allen-Cahn equation

$$\frac{\partial \mathbf{u}}{\partial t} = L(\mathbf{u}) \left( \kappa_{\text{pf}} \Delta \mathbf{u} - \frac{\partial W(\mathbf{u})}{\partial \mathbf{u}} \right), \quad (1)$$

where the vector phase-field variable  $\mathbf{u} = \{u_1, u_2, \dots, u_p\}$ ,  $L$  and  $\kappa_{\text{pf}}$  are model parameters. The multiwell potential  $W$  has the following form [12]:

$$W(\mathbf{u}) = w \left[ \sum_{\alpha=1}^p \left( \frac{u_\alpha^4}{4} - \frac{u_\alpha^2}{2} \right) + \sum_{\alpha=1}^p \sum_{\beta>\alpha}^p \sigma_{\alpha\beta} u_\alpha^2 u_\beta^2 + \frac{1}{4} \right], \quad (2)$$

where  $w$  and  $\sigma_{\alpha\beta}$  are model parameters. In this work,  $\sigma_{\alpha\beta} = 1.5$  in order to have a symmetric profile. The misorientation dependence of mobility is taken into account in the  $L$  parameter [15]:

$$L(\mathbf{u}) = \frac{\sum_{\alpha\beta} L_{\alpha\beta} u_\alpha^2 u_\beta^2}{\sum_{\alpha\beta} u_\alpha^2 u_\beta^2}, \quad (3)$$

where  $L_{\alpha\beta}$  is related to the reduced grain boundary mobility  $m_{\alpha\beta}$  (between grains  $\alpha$  and  $\beta$ ) by

$$L_{\alpha\beta} = \frac{4m_{\alpha\beta}}{3l_{\text{gb}}}. \quad (4)$$

Here  $l_{\text{gb}}$  is the width of the diffusion (grain) boundary, which is controlled by model parameters  $\kappa_{\text{pf}}$  and  $w$  by

$$l_{\text{gb}} = \sqrt{\frac{8\kappa_{\text{pf}}}{w}}. \quad (5)$$

In this work, the grain boundary width  $l_{\text{gb}}$  is chosen to be 4 grid points based on the previous analysis [41]. For the model used here, phase-field parameters  $\kappa_{\text{pf}}$  and  $w$  are related by  $\sqrt{2\kappa_{\text{pf}}w} = 3$ .

The phase-field equation (Eq. (1)) is solved on an NVIDIA Tesla V100 GPU with the active parameter tracking (APT) algorithm [42,43]. The numerical implementation of the model outlined above has been carefully and successfully tested against known analytical solutions for various geometries, which is detailed in Ref. [44]. Details on numerical implementation are provided in supplementary materials and Ref. [44].

More advanced phase-field models can be introduced, which, for example, include the dependence on grain boundary inclination of energy and mobility [16]. Notably, the good correspondence between the grain boundaries provided by our simple model and experimental data, as will be shown in Section 3, implies that such more advanced phase-field models can at best provide incremental improvements, and will therefore not influence the conclusions of this work. In addition, such models are significantly more complex, and as a result, the computational cost will increase dramatically both for the phase-field simulation and for the fitting (a reinitialization process is needed to connect the phase-field variable and the signed distance function, see Section S3.1 in supplementary materials for details).

### 2.3. Fitting method

The fitting methodology is illustrated in Fig. 1: it combines a 3D experimental movie of the grain growth with 3D phase-field simulations. The reduced mobilities  $\mathbf{m} = \{m^1, m^2, \dots, m^n\}$ , where  $n$  is the number of grain boundaries in the system, are iteratively refined until the simulation optimally matches the experiment. Theoretically, the reduced mobility of all grain boundaries in the sample can be determined in this way, as well as their time dependence (if any). Notably, this global fitting procedure avoids measuring the local

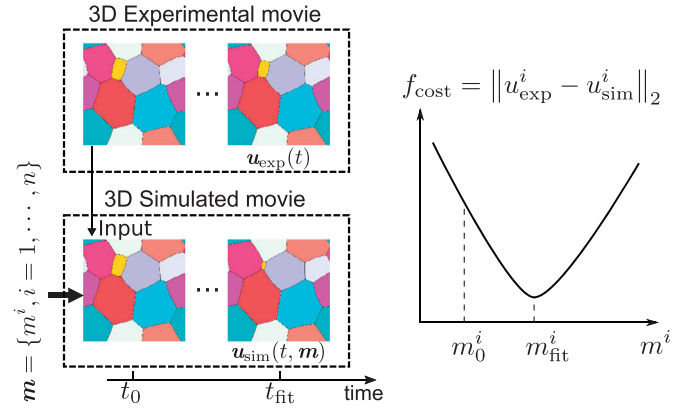


**Fig. 1.** Schematic diagram of the fitting method. The 3D position of grain boundaries,  $\mathbf{u}_{\text{exp}}(t)$ , is determined experimentally as a function of time,  $t$ . Using one time-step  $t_0$  of the experimental movie as the initial configuration, a 3D simulated microstructure  $\mathbf{u}_{\text{sim}}(t, \mathbf{m})$  is generated by a phase-field model with an initial guess of the reduced mobility  $m^i$  of each boundary  $i$ . At a later time-step  $t_{\text{fit}}$ , the simulated microstructure is compared with the experimental one, and a cost function  $f_{\text{cost}}$  is defined to quantify the difference between the experiment and the simulation,  $\|\cdot\|_2$  is the  $L_2$  norm. The cost function is minimized to find the set of reduced mobilities  $m_{\text{fit}}^i$  of each boundary that provide a best match between the simulation and the experiment.

velocity and the difficult-to-measure curvature along the boundary. Moreover, the effect of the morphology and topology of the grain network on the migration of individual boundaries is accounted for in the phase-field model, thus also in the fitting process.

#### 2.3.1. Mathematical formulation

Formally, the fitting procedure can be described as an optimization problem

$$\begin{aligned} & \text{find } \mathbf{m} = \{m^1, m^2, \dots, m^n\} \\ & \text{minimize } f_{\text{cost}}(t, \mathbf{m}) = \sum_{\alpha\beta} f_{\text{cost}}^{\alpha\beta} \\ & \text{such that } \mathbf{u}_{\text{sim}}(t_0, \mathbf{m}) = \mathbf{u}_{\text{exp}}(t_0) \\ & \quad \mathbf{u}_{\text{sim}}(t, \mathbf{m}) \text{ follows Eq. (1)}, \end{aligned} \quad (6)$$

where  $t$  is time, and  $\alpha\beta$  symbolizes the grain boundary shared by grains  $\alpha$  and  $\beta$ . The cost function  $f_{\text{cost}}$  measures the difference between the positions of the grain boundaries in the simulated microstructure  $\mathbf{u}_{\text{sim}}$  and the position of the grain boundaries in the experimental microstructure  $\mathbf{u}_{\text{exp}}$ . The cost function is defined as the summation over all grain boundaries of the local cost functions  $f_{\text{cost}}^{\alpha\beta}$ . The local cost function related to the grain boundary between grains  $\alpha$  and  $\beta$  is defined as

$$\begin{aligned} f_{\text{cost}}^{\alpha\beta} & \left( u_{\text{sim}}^\alpha, u_{\text{sim}}^\beta, \phi_{\text{exp}}^\alpha, \phi_{\text{exp}}^\beta \right) \\ & = \int_{\Gamma^{\alpha\beta}} \left( \phi(u_{\text{sim}}^\alpha) - \phi_{\text{exp}}^\alpha \right)^2 + \left( \phi(u_{\text{sim}}^\beta) - \phi_{\text{exp}}^\beta \right)^2 dx, \end{aligned} \quad (7)$$

where the integral domain  $\Gamma^{\alpha\beta}$  is the region spanned by grain boundary  $\alpha\beta$ . In this work, as the grain boundary is diffuse in the phase-field model,  $\Gamma^{\alpha\beta}$  is a narrow band near the grain boundary.  $\phi_{\text{exp}}$  is the signed-distance function determined from the experiment,  $\phi(u)$  is the signed-distance function corresponding to the phase-field variable,  $u$  (supplementary materials Section S3.1). As shown in Section S3.4 of supplementary materials, the triple-junction region  $\Omega_{\text{ij}}$  is excluded from the fitting domain  $\Omega_{\text{fit}}^{\alpha\beta} = \Gamma^{\alpha\beta} \setminus \Omega_{\text{ij}}$ . The local cost function in Eq. (7) is then calculated as

$$\begin{aligned} f_{\text{cost}}^{\alpha\beta} & \left( u_{\text{sim}}^\alpha, u_{\text{sim}}^\beta, \phi_{\text{exp}}^\alpha, \phi_{\text{exp}}^\beta \right) \\ & = \int_{\Omega_{\text{fit}}^{\alpha\beta}} \left( \phi(u_{\text{sim}}^\alpha) - \phi_{\text{exp}}^\alpha \right)^2 + \left( \phi(u_{\text{sim}}^\beta) - \phi_{\text{exp}}^\beta \right)^2 dx. \end{aligned} \quad (8)$$

Sensitivity analysis (see Section S3.2 of supplementary materials) of the optimization problem reveals that the original optimization

problem in Eq. (6) can be approximated by a series of easy-to-solve sub-problems. For each grain boundary  $\alpha\beta$ , the sub-problem is defined as the minimization problem

$$\begin{aligned} & \text{find } L_{\alpha\beta} \\ & \text{minimize } f_{\text{cost}}^{\alpha\beta}(t, L_{\alpha\beta}) \\ & \text{such that } \mathbf{u}_{\text{sim}}(t_0, \mathbf{m}) = \mathbf{u}_{\text{exp}}(t_0) \\ & \quad \mathbf{u}_{\text{sim}}(t, \mathbf{m}) \text{ follows Eq. (1).} \end{aligned} \quad (9)$$

As a consequence of this approximation, within each iteration of the fitting procedure, we replace the multidimensional fit to all reduced mobilities by independent one-dimensional fits to the individual reduced mobilities. Notice that the sub-problems are just an approximation of the original optimization problem, therefore, an iterative fitting process is required. Details of the fitting algorithm, sensitivity analysis are provided in supplementary materials.

### 2.3.2. Initial guess

The initial guess used for the reduced mobilities is  $m_i^0 = 0.1 \mu\text{m}^2/\text{s}$ ,  $\forall i$ . This number represents the grain averaged reduced mobility, see Ref. [37]. Numerical results show that the fitting algorithm is not sensitive to the initial guess of the reduced mobility.

### 2.3.3. Convergence check

A typical convergence of one grain boundary in the fitting of the experimental data is shown in Fig. 2. Numerical tests showed that the proposed fitting algorithm in general converges very fast (see Fig. 2b); thus, we fix the total number of the fitting iterations to 10.

### 2.3.4. Fitting quality

Fig. 3 shows an example of the quality of the fit. The close correspondence of the boundary morphologies between experiment and simulation indicates that the local variation of the reduced mobility along the grain boundary is small. A detailed analysis of the fitted reduced mobilities will be presented in the next section.

## 3. Results

As presented in Section 2.3 we fit every boundary with a non-zero fitting domain (the size of  $\Omega_{\text{fit}}^{\alpha\beta}$  needs to be at least one voxel to calculate the local cost function in Eq. (8)). This set includes essentially all boundaries in the system, with the prime exceptions being cases of disappearing or newly formed boundaries due to topological changes taking place between  $t_0$  and  $t_{\text{fit}}$ . We fitted the reduced mobilities for 35 different combinations of  $(t_0, t_{\text{fit}})$ , see Table 1, resulting in 149,547

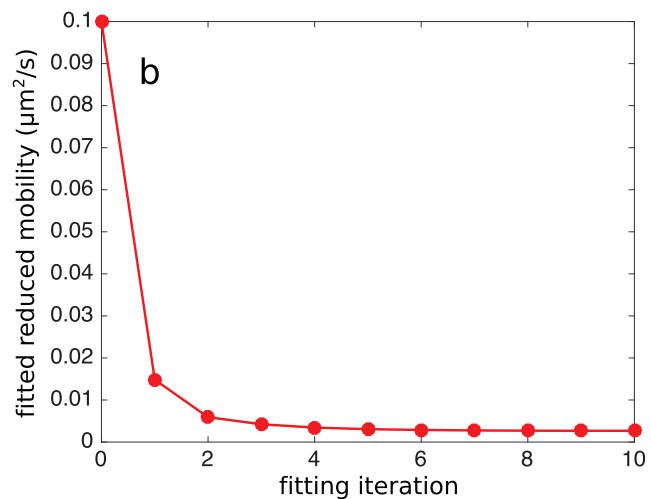
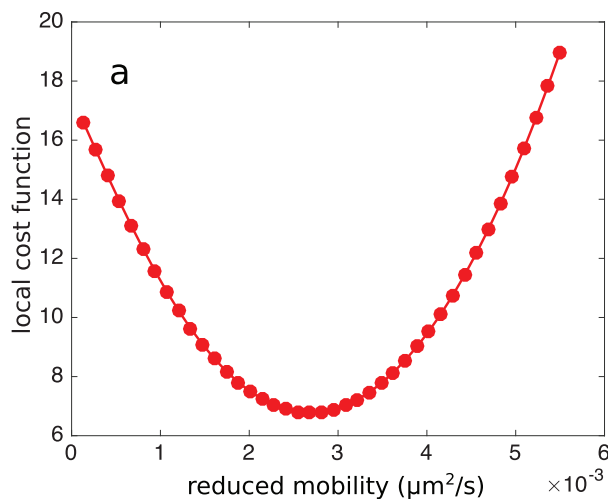


Fig. 2. Typical fitting curves. (a) the local cost function for one iteration and one grain boundary, and (b) the convergence of the fitted reduced mobility for this boundary based on the experimental data and the proposed fitting algorithm. The local cost function shown in (a) corresponds to the fitting iteration 10 in (b).

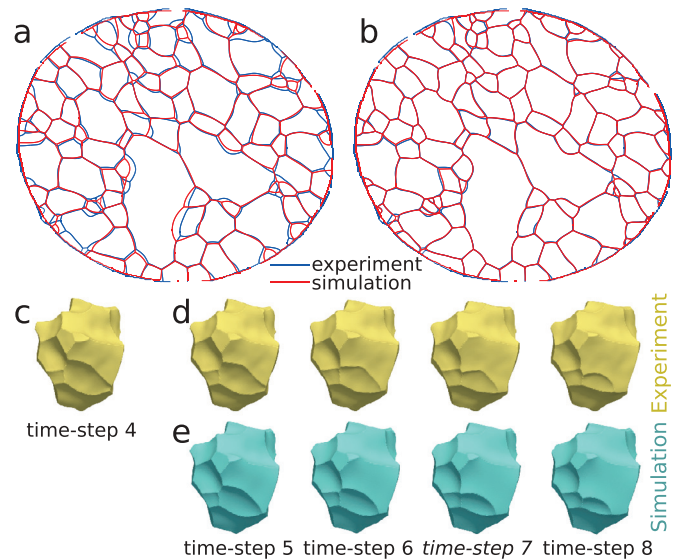


Fig. 3. Quality of the data and the fit. Comparison of the experimental and the simulated grain boundaries at time-step 7 within one slice of the 3D volume, (a) with the simulation starting from time-step 4 and ending at time-step 7 with the initial guess of the reduced mobilities. (b) The same with optimized/fitted reduced mobilities. (c) A grain at time-step 4. Its morphology at later time-steps as (d) determined experimentally and (e) simulated with the optimized reduced mobilities. See supplementary videos 3 and 4 for details in convergence.

reduced mobilities. Notice that the immediate next time step is not used as most boundaries do not move a sufficiently large distance to enable an accurate fitting. In the following, we provide a detailed analysis of the fitted reduced mobilities.

### 3.1. Fitted reduced mobilities as a function of the 5D space

Not all fitted values were equally reliable due to several factors, therefore, the following criteria were applied to select the most reliable fitting results:

1. The boundary condition used in the phase-field calculation is similar to a pinned boundary condition, which may or may not be different from the physical boundary condition in the experiment [44]. Thus, we do not include the reduced mobilities of boundaries that are connected to the exterior in our data set.

**Table 1**  
The 35 combinations of ( $t_0, t_{fit}$ ) used in fitting the reduced mobilities.

$t_0$	$t_{fit}$													
2	4	-	-	-	-	-	-	-	-	-	-	-	-	-
3	-	5	6	7	-	-	-	-	-	-	-	-	-	-
4	-	-	6	7	8	9	10	-	-	-	-	-	-	-
5	-	-	-	7	8	9	10	-	-	-	-	-	-	-
6	-	-	-	-	8	9	10	11	-	-	-	-	-	-
7	-	-	-	-	-	9	10	11	12	-	-	-	-	-
8	-	-	-	-	-	-	10	11	12	13	14	-	-	-
9	-	-	-	-	-	-	-	11	12	13	14	-	-	-
10	-	-	-	-	-	-	-	-	12	13	14	-	-	-
11	-	-	-	-	-	-	-	-	-	13	14	-	-	-

However, since the triple-line formed between these boundaries and the interior boundaries are moving in a manner consistent with the experiment (these boundaries are involved in the fitting process), we include in the data set interior boundaries that are connected to boundaries touching the exterior surface.

- Boundaries where the fitting did not converge after 10 fitting iterations are removed.
- Boundaries that moved a distance that is not sufficiently large compared to the experimental uncertainty on boundary position are excluded. We choose a threshold of  $0.5\Delta x$  ( $\Delta x$  is the voxel size) to balance the accuracy and grain boundary statistics.
- Boundaries with an area that is too small in the fitting domain  $\Omega_{fit}^{\alpha\beta}$  are excluded. We choose a threshold of  $10\Delta x^2$ .
- Boundaries that are connected to boundaries that follow criteria 3 and 4 are excluded in order to prevent any influence from badly fitted neighboring boundaries.
- To quantify the quality of the fitting for each boundary  $\alpha\beta$ , we introduce as a figure-of-merit:

$$\delta_{\alpha\beta}(t_{fit}, t_0) = \sqrt{\frac{\int_{\Omega_{fit}^{\alpha\beta}} (\phi_{sim}^\alpha(t_{fit}) - \phi_{exp}^\alpha(t_{fit}))^2 + (\phi_{sim}^\beta(t_{fit}) - \phi_{exp}^\beta(t_{fit}))^2 dx}{\int_{\Omega_{fit}^{\alpha\beta}} (\phi_{exp}^\alpha(t_{fit}) - \phi_{exp}^\alpha(t_0))^2 + (\phi_{exp}^\beta(t_{fit}) - \phi_{exp}^\beta(t_0))^2 dx}} \quad (10)$$

It measures the ratio of the distance difference of the simulated and experimental boundary with respect to the distance traveled in the experiment from  $t_0$  to  $t_{fit}$ . For a complete match between the experiment and the simulation,  $\delta_{\alpha\beta}$  has zero value. Larger value of  $\delta_{\alpha\beta}$  means poorer fit. In this work, we removed all boundaries with  $\delta_{\alpha\beta} > 0.5$ .

Applying the six criteria listed above, this procedure resulted in 10,307 reduced mobilities of 1,619 boundaries.

To further improve the quality of the data set used, we choose to include only those boundaries which exhibit at least 5 reliable measurements (fulfill all six criteria) out of the 35 fittings and a small variation of the reduced mobility over time (maximum divided by minimum less than five). These boundaries are represented only once, with an average value over the repeated measurements. We further removed highly curved boundaries (average change in the normal to the boundary larger than 25 degrees), consistent with our assumption that reduced mobility is a constant along a boundary, and boundaries having a large change in inclination with time (change in averaged boundary normal with time larger than 15 degrees), since they cannot be categorized as the same boundary with a close five macroscopic degrees of freedom. This yields the reduced mobilities of the 344 boundaries, which are displayed in Fig. 4. A 3D visualization of the data in the fundamental zone of the Rodrigues–Frank space can be seen in the supplementary video 5. Fig. 4a shows that the reduced mobility varies by three orders of magnitude, with no clear correlation with the misorientation angle.

The values of measured reduced mobilities are consistent with the range of average reduced mobilities determined from a measurement of average grain sizes [37]. Fig. 4b and 4c reveal that there is no apparent correlation with any of the five macroscopic degrees of freedom related to crystallography. As the boundary energy is known to be a function of crystallography and to vary by much less than shown in Fig. 4 [7], we conclude that the grain boundary mobilities are generally uncorrelated with the crystallography. Consistent with this lack of correlation with crystallography, we have identified two boundaries where all five crystallographic parameters are very similar, yet have reduced mobilities that are different by a factor of 9 (see Section S3.6 in supplementary materials).

Note that 344 data points are not sufficient to populate the 5D space; thus Fig. 4 shows three projections of the 5D space. We have explored loosening the criteria in several ways, thereby increasing the number of boundaries. In all cases the conclusion remains the same: there is no evidence for a strong correlation with the boundary crystallography.

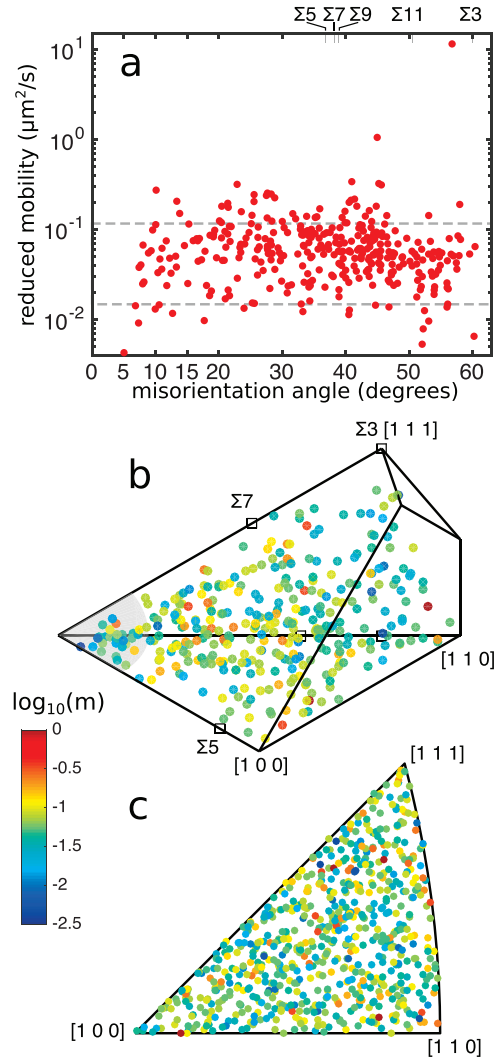


**Fig. 4.** Results of the fitted reduced mobilities. The logarithm of the reduced mobility as a function of (a) misorientation angle, (b) misorientation (Rodrigues–Frank space) and (c) grain boundary inclination. Three special boundaries ( $\Sigma 3$ ,  $\Sigma 5$ , and  $\Sigma 7$ ) and the region of low angle boundaries (grey region, corresponding to 15 degrees) are marked in (b). In (a) the grey dashed lines show the full range of the grain-averaged reduced mobilities measured in our previous statistical analysis of this grain growth process [37].

### 3.2. Low-velocity boundaries

The analysis reported in Section 3.1 and results shown in Fig. 4 are based on a set of grain boundaries, which were chosen based on certain selected criteria. Amongst these is criterion 3: boundaries should move a distance that is sufficiently large compared to the experimental uncertainty on boundary position. In a complementary search of the database of all reduced mobilities we here test to what extent boundaries with a very small velocity are correlated with crystallography. In this case, we define the set of valid boundaries by criteria:

1. The boundary is not connected to the sample surface.
2. The delta parameter Eq. (10) less than 1.
3. The distance moved is less than 0.3 voxel size.
4. The fitted reduced mobility is less than  $0.01 \mu\text{m}^2/\text{s}$ .
5. The fitting converged.

These five criteria result in 191 reduced mobilities. Fig. 5 shows the identified boundaries in the fundamental zone of the Rodrigues–Frank space. There are 20 low angle boundaries with a misorientation angle of smaller than 15 degrees and three  $\Sigma 3$  boundaries. For these special grain boundaries, we observed a correlation with small grain boundary velocity (Fig. 5). For all other boundaries - the vast majority - we find no correlation with the crystallographic parameters.

### 3.3. Time-variation of the reduced mobility

Another characteristic of the data is that the reduced mobilities vary in time, which is in contrast to conventional understanding because the crystallographic character of the boundary does not change significantly. To improve statistics, we average the fitted reduced mobility within two sets of  $(t_0, t_{\text{fit}})$ , respectively, see Tables S1 and S2 for details. The averaged reduced mobility of the set 1 (using early time-steps) is denoted as  $m_{\text{early}}$  and the averaged reduced mobility of set 2 (later time-steps) is denoted as  $m_{\text{late}}$ . To make sure only the high-quality points are used in this study, we apply the following criteria (in addition to the six criteria established in Section 3.1) to select the points used for the average:

1. The ratio of the maximum value of the fitted reduced mobilities over the minimum value within each set is less than 5.
2. At least 3 good points can be used to calculate the average.
3. The same boundary is present in both set 1 and set 2.

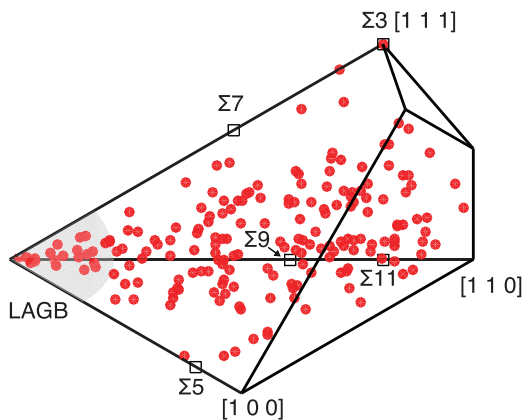


**Fig. 5.** Boundaries with small reduced mobility shown in the fundamental zone of the Rodrigues–Frank space. The region comprising low angle grain boundaries (LAGB) with misorientation angles  $\leq 15$  degrees are shown by the grey region. Five types of special boundaries,  $\Sigma 3$ ,  $\Sigma 5$ ,  $\Sigma 7$ ,  $\Sigma 9$ , and  $\Sigma 11$ , are marked by square symbols. See supplementary video 6 for a 3D view of the data.

Applying these criteria, we identified 168 boundaries, with the data of  $m_{\text{early}}$  and  $m_{\text{late}}$  showed in Fig. 6. Fig. 7 plots the distribution of the ratio  $m_{\text{late}}/m_{\text{early}}$  of same boundaries. While grain-averaged parameters are continuously declining [37], the reduced mobilities for some boundaries are decreasing while others are increasing, which would rule out solute drag as responsible for the decline in average reduced mobility. Note that the misorientation between grain boundaries does not change with time (no grain rotation observed during growth within the experimental resolution, *i.e.*, 0.1 degrees). Moreover, the change in reduced mobility is not correlated with the change in inclination, as shown in Fig. 6b. The large variations with time, therefore, provides more evidence that the grain boundary mobilities are not uniquely determined by the boundary's five macroscopic degrees of freedom and additional physics, perhaps on processes on an atomistic scale, are needed to fully describe the reduced grain boundary mobility.

### 3.4. A possible connection between a change in reduced mobility and a topological change

Grain growth involves topological changes, where grain neighbor relationships are changed and potentially some grains disappear [37,45]. In connection with the time-variation of the reduced mobility presented in Section 3.3, in particular, we find evidence that topological changes in the grain boundary network can lead to sudden jumps in reduced mobility by more than an order of magnitude. Within the data set, we identified 13 cases where a marked change in reduced mobility appears in connection with such topological changes. Here, we report on a detailed analysis of two of them.

In the first case, as shown in Fig. 8, the boundary 1-2 between grains 1 and 2 moved a very small distance from time-step 1 to time-step 3, a period in time where the adjacent triple-line moves in a

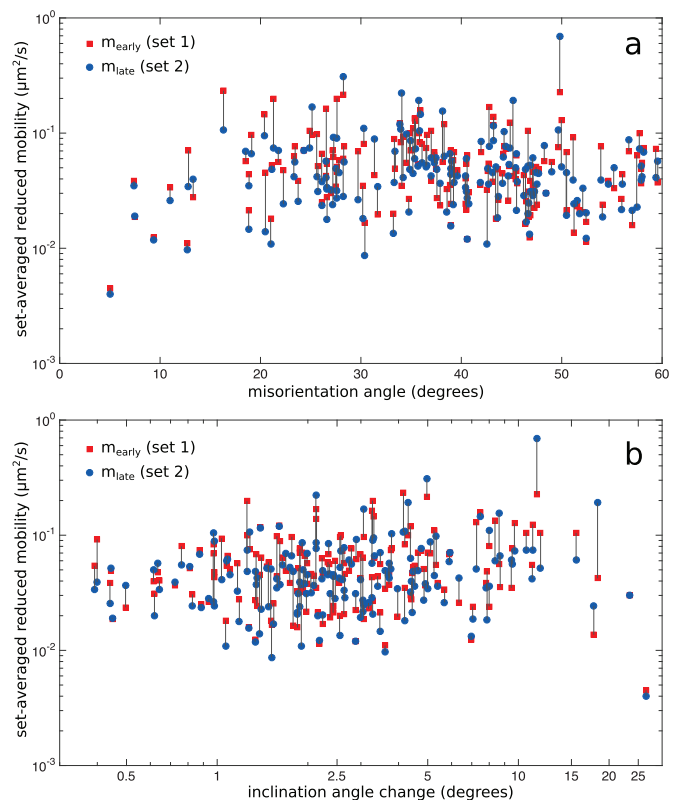


**Fig. 6.** Time-variation of reduced mobilities of individual boundaries. The set-averaged reduced mobility as a function of (a) the misorientation angle and (b) the inclination angle change between two sets. Set 1 is at an early stage of the grain growth and set 2 is at a late stage. The grey line connects data points of the same boundary.

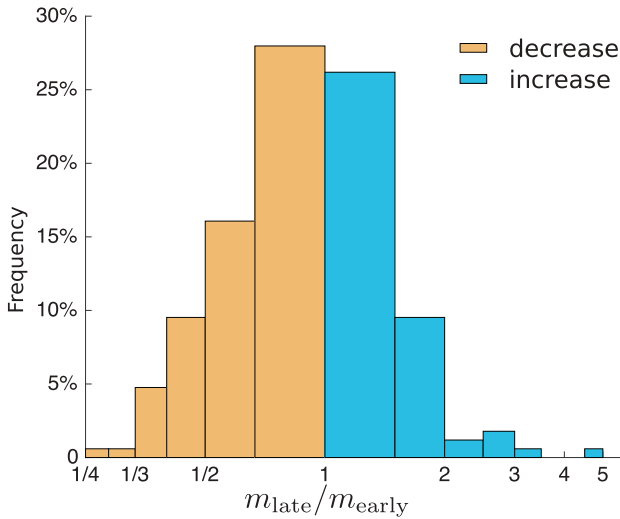


**Fig. 7.** Time-variation of the individual reduced mobilities. The frequency of finding boundaries with reduced mobilities that have decreased (brown) and those that have increased (blue). A logarithm scale is used on the x-axis to ease visualization.

direction parallel to the grain boundary. Grain 3 disappeared between time-step 3 and time-step 4. After this topological change, the grain boundary 1-2 starts to move very quickly, as shown in the contour plot in Fig. 8.

In order to provide a more comprehensive analysis, we changed the fitting procedure. Instead of making fits to all boundaries in the system (at each iteration step) we fitted all boundaries within a cluster of grains (grains 1 and 2 and their first neighbors) simultaneously. This local fitting is fast compared to the fitting of all reduced mobilities within the full sample volume (1501 grains) and allows a detailed and more accurate fitting of the grain boundary 1-2. This local fitting can help to exclude the possibility that the velocity change is due to a change in the curvature of the boundary. Here  $t_0$  and  $t_{\text{fit}}$  are chosen to make sure there is no topological change between  $t_0$  and  $t_{\text{fit}}$ . Time-step 5 has a relatively large experimental error; therefore, not involved in the local fitting. The local fitting results with different combinations of ( $t_0$ ,  $t_{\text{fit}}$ ) are listed in Table 2 and the simulation with the optimized reduced mobility values is compared with the

**Table 2**  
Time-variation of the fitted reduced mobility for the grain boundary between grain 1 and 2 in Fig. 8. A simultaneous fit was here performed to all grain boundaries within a local cluster of grains.

$t_0$	$t_{\text{fit}}$	$m_{\text{fit}} (\mu\text{m}^2/\text{s})$
2	3	0.01
4	6	0.15
4	7	0.31

experiment in Fig. 9a. It can be seen that the reduced mobility after the topological change is more than an order of magnitude larger than the reduced mobility before the topological change. Next, we performed a simulation that started at time-step 2 and ran until time-step 7. In this simulation, the reduced mobility of the grain boundary 1-2 at time-steps 2 and 3 is fixed at  $0.01 \mu\text{m}^2/\text{s}$ , while it is fixed at  $0.3 \mu\text{m}^2/\text{s}$  after the topological change. The reduced mobilities of the rest boundaries are manually tuned based on the local fitting results with the three combinations of ( $t_0$ ,  $t_{\text{fit}}$ ) in Table 2. It can be seen from Fig. 9b that this two-step model provides a relatively good match between the experiment and the simulation for almost all the time-steps, including the correct prediction of the topological change. Notice that with a single value of the reduced mobility of grain boundary 1-2, we cannot get a reasonable match between the experiment and the simulation for both time-steps before and after the topological change. This means the jump in the reduced mobility is likely to be related to the topological change. However, in this case, the inclination angle of part of the boundary changes about 15 - 20 degrees after the topological event. Notably, there is also inclination change in the phase-field simulation although there is no inclination dependence of the reduced mobility in the simulation (Fig. 9b).

The second case illustrating the potential relationship between reduced mobility and topological change is summarized in Fig. 10. In this case, the topological event happens between time-step 7 and time-step 8. Within the experimental error, the repeated measurements clearly show a two-stage movement of the grain boundary coincident with the topological change, see Fig. 10b. The grain boundary has small velocity both before (time-steps 4-6) and after (time-steps 9-15) the topological change. However, during the period including the topological change, the reduced mobility is more than an order of magnitude larger. Notably, in this case, the inclination

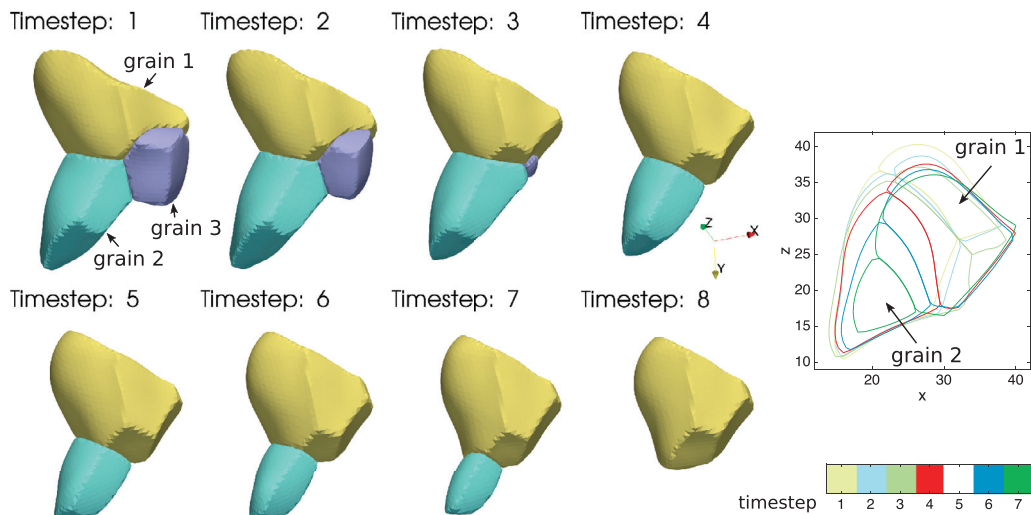


**Fig. 8.** Evolution of a grain boundary (between grains 1 and 2) in connection with a topological change (grain 3 disappears between time-steps 3 and 4). The figure to the right shows the evolution of the boundaries of grains 1 and 2 within one slice in the x-z plane. Here time-step 5 is omitted due to a relatively larger uncertainty on the experimental data for this particular boundary.

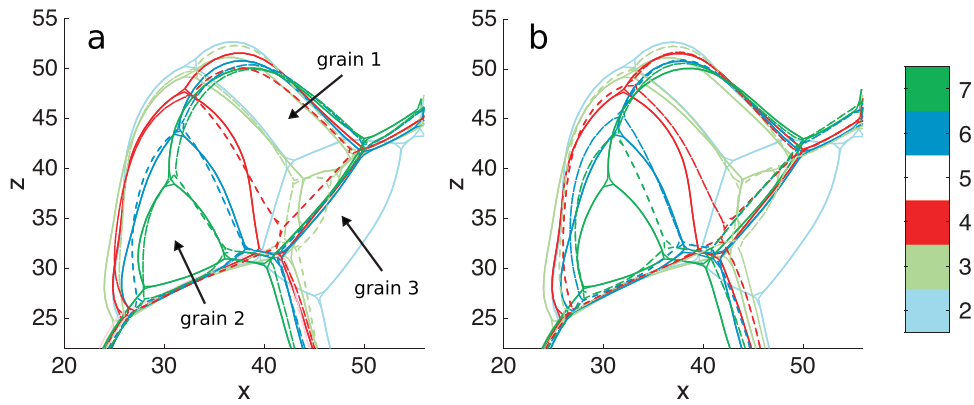


**Fig. 9.** Comparison between experiment (solid lines) and two types of simulations (dashed lines) for the topological change depicted in Fig. 8. (a) Simulations at time-step  $t_{fit}$  with the resulting optimized reduced mobilities from local fittings in Table 2. (b) A two-step model running from time-step 2 to time-step 7. In both cases, time-step 5 is omitted due to a relatively larger uncertainty on the experimental data. The unit of axes is voxel size. Contours in the 2D section for various time-steps are identified by the bar to the right.

does not change significantly, as evidenced by Fig. 10a. The other 11 cases have not been analyzed to the same level of detail. However, based on inspection these cases are consistent with the conjecture that reduced mobilities are influenced by topological changes.

These observations as well as those of Fig. 4, demonstrate that the grain growth behavior for the large majority of boundaries is governed by mechanisms other than those underlying the classical models of grain growth.

#### 4. Discussion

The results reveal that the reduced grain boundary mobilities vary by at least three orders of magnitude. Two grain boundaries with approximately the same five macroscopic degrees of freedom can exhibit radically different migration behavior. Clearly, some critical physics is missing to fully describe the grain boundary migration process. There are various possibilities regarding the missing degrees of freedom. Triple junction drag due to a low triple junction mobility has been observed for nano-scale grains [46,47], but it is unlikely that it can explain the dramatic change in the reduced mobility in this case. Instead, we see evidence that a change in reduced mobility may be connected to the topological change that occurs when grain faces are created or removed. However, other physics can be operative that may explain the lack of correlation, such as nanoscale grain

boundary facets [48], disconnections [21–24], grain interior defects [49], elastic strain [50], and other atomistic scale processes.

In the future, unraveling the microscopic origin of the reduced mobility variation may benefit from new multiscale 3D x-ray imaging methods, that will allow us to zoom into individual grains [51,52], and map dislocations [53], and local strain with a resolution of 30–100 nm [54]. The development of high-performance computing can help to speed up the simulations and allow the use of more advanced phase-field models. Phase-field models with inclination dependence will allow us to analyze the highly curved boundaries that were removed from the data set. The presented fitting methodology may also be extended to determine the triple junction mobilities for nanocrystalline materials with the help of higher resolution x-ray imaging methods [51,52,54] and suitable phase-field models [47].

#### 5. Conclusions

In this work, we have developed a rapid throughput fitting methodology to determine reduced grain boundary mobilities by comparison between time-resolved diffraction contrast tomography experiment of a polycrystalline sample and phase-field simulations of grain growth. The proposed fitting methodology is a global fitting process, therefore avoids measuring the local grain boundary velocity and curvature, which in practice are difficult to be measured accurately. The effect of neighboring boundaries on grain boundary migration is accounted for by the phase-field method. We have applied the fitting method to a pure iron grain growth data set and determined 10,307 reduced mobilities of 1619 boundaries. A detailed analysis of the measured reduced mobilities versus the five macroscopic degrees of freedom of grain boundaries shows no evidence of a strong correlation between reduced grain boundary mobilities and the crystallography of the boundaries. Moreover, we observed that the reduced mobility of a grain boundary can vary in time and may be affected by topological changes. All these observations imply that grain boundary motion in polycrystals is governed by factors other than the crystallography of the grain boundary.

Predicting the time evolution of the microstructure during processing is a prerequisite to attaining the vision of “materials design based on simulations” [55]. We argue that our results are relevant for most applications - with industrial materials not being ultra-pure - and hence demonstrating the need for a new generation of multiscale models for describing grain growth. The data comprises a comprehensive testbed for validating new mechanisms.

Directly comparing 3D experimental movies and 3D simulations is an approach that can be used in many other fields in materials science, e.g., plastic deformation and phase transformations. With hundreds of millions of points in space-time, this approach can guide

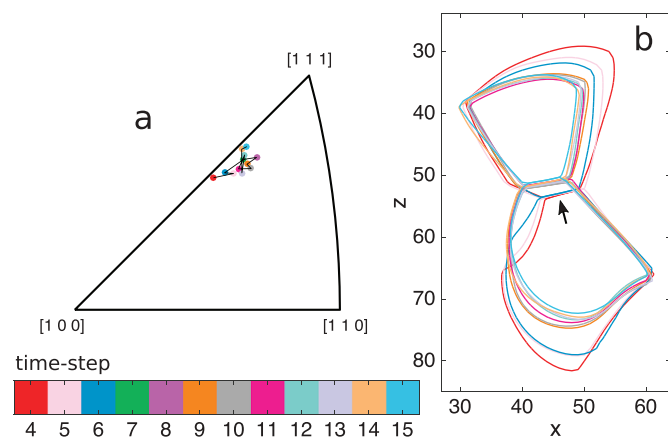


**Fig. 10.** Inclination character and evolution of microstructure of one boundary. The evolution of (a) inclination as a function of time-steps of the grain boundary shown in (b) (marked by the arrow). Time-steps 7 and 8, which are related to the topological event, are not shown in (b) to ease the visualization of the two-stage movement of the grain boundary. The unit of axes in (b) is voxel size. Contours in the 2D section at various time-steps are identified by the bar below.

theory and validate models in an unprecedented way. In particular, in favorable cases all relevant materials parameters can be extracted from one experiment using representative samples and processing tools.

### Declaration of Competing Interest

The authors declare that they have no known competing financial interests or personal relationships that could have appeared to influence the work reported in this paper.

### Acknowledgments

This study was supported by grants from the Danish Innovation Fund for the center CINEMA [1305-00032B], National Institute for Standards and Technology through the Center for Hierarchical Materials Design contract [70NANB19H00], Office of Naval Research and The US Naval Research Laboratory [N0001415WX00004]. We thank Danscatt [7055-00005B] for travel support and ESRF for beamtime [HC2933]. We thank the use of computing resources at the DTU Computing Center.

### Supplementary material

Supplementary material associated with this article can be found in the online version at doi:[10.1016/j.actamat.2020.03.044](https://doi.org/10.1016/j.actamat.2020.03.044)

### References

- [1] J. Von Neumann, Discussion: Shape of metal grains, *Metal Interfaces* (1952) 108.
- [2] W.W. Mullins, Two-dimensional motion of idealized grain boundaries, *J. Appl. Phys.* 27 (8) (1956) 900–904, doi: [10.1063/1.1722511](https://doi.org/10.1063/1.1722511).
- [3] R.D. MacPherson, D.J. Srolovitz, The von Neumann relation generalized to coarsening of three-dimensional microstructures, *Nature* 446 (7139) (2007) 1053, doi: [10.1038/nature05745](https://doi.org/10.1038/nature05745).
- [4] A.P. Sutton, R.W. Balluffi, A. Sutton, *Interfaces in Crystalline Materials*, Clarendon Press Oxford, 1995.
- [5] G. Gottstein, L.S. Shvindlerman, *Grain Boundary Migration in Metals: Thermodynamics, Kinetics, Applications*, CRC Press, 2009.
- [6] G.S. Rohrer, Grain boundary energy anisotropy: a review, *J. Mater. Sci.* 46 (18) (2011) 5881–5895, doi: [10.1007/s10853-011-5677-3](https://doi.org/10.1007/s10853-011-5677-3).
- [7] S. Ratanaphan, D.L. Olmsted, V.V. Bulatov, E.A. Holm, A.D. Rollett, G.S. Rohrer, Grain boundary energies in body-centered cubic metals, *Acta Materialia* 88 (2015) 346–354, doi: [10.1016/j.actamat.2015.01.069](https://doi.org/10.1016/j.actamat.2015.01.069).
- [8] G. Gottstein, D. Molodov, L. Shvindlerman, D. Srolovitz, M. Winning, Grain boundary migration: misorientation dependence, *Current Opin. Solid State Mater. Sci.* 5 (1) (2001) 9–14, doi: [10.1016/S1359-0286\(00\)00030-9](https://doi.org/10.1016/S1359-0286(00)00030-9).
- [9] A. Rollett, G. Gottstein, L. Shvindlerman, D. Molodov, Grain boundary mobility—a brief review, *Zeitschrift Für Metallkunde* 95 (4) (2004) 226–229, doi: [10.3139/146.017938](https://doi.org/10.3139/146.017938).
- [10] L.-Q. Chen, Phase-field models for microstructure evolution, *Ann. Rev. Mater. Res.* 32 (1) (2002) 113–140, doi: [10.1146/annurev.matsci.32.112001.132041](https://doi.org/10.1146/annurev.matsci.32.112001.132041).
- [11] I. Steinbach, Phase-field model for microstructure evolution at the mesoscopic scale, *Ann. Rev. Mater. Res.* 43 (2013) 89–107, doi: [10.1146/annurev-matsci-071312-121703](https://doi.org/10.1146/annurev-matsci-071312-121703).
- [12] L.-Q. Chen, W. Yang, Computer simulation of the domain dynamics of a quenched system with a large number of nonconserved order parameters: the grain-growth kinetics, *Phys. Rev. B* 50 (21) (1994) 15752, doi: [10.1103/PhysRevB.50.15752](https://doi.org/10.1103/PhysRevB.50.15752).
- [13] A. Kazaryan, Y. Wang, S. Dregia, B. Patton, Grain growth in anisotropic systems: comparison of effects of energy and mobility, *Acta Materialia* 50 (10) (2002) 2491–2502, doi: [10.1016/S1359-6454\(02\)00078-2](https://doi.org/10.1016/S1359-6454(02)00078-2).
- [14] N. Moelans, B. Blanpain, P. Wollants, Quantitative phase-field approach for simulating grain growth in anisotropic systems with arbitrary inclination and misorientation dependence, *Phys. Rev. Lett.* 101 (2) (2008) 25502, doi: [10.1103/PhysRevLett.101.025502](https://doi.org/10.1103/PhysRevLett.101.025502).
- [15] N. Moelans, A quantitative and thermodynamically consistent phase-field interpolation function for multi-phase systems, *Acta Materialia* 59 (3) (2011) 1077–1086, doi: [10.1016/j.actamat.2010.10.038](https://doi.org/10.1016/j.actamat.2010.10.038).
- [16] H.-K. Kim, S.G. Kim, W. Dong, I. Steinbach, B.-J. Lee, Phase-field modeling for 3D grain growth based on a grain boundary energy database, *Model. Simul. Mater. Sci. Eng.* 22 (3) (2014) 34004, doi: [10.1088/0965-0393/22/3/034004](https://doi.org/10.1088/0965-0393/22/3/034004).
- [17] H. Garcke, B. Nestler, B. Stoth, A multiphase field concept: numerical simulations of moving phase boundaries and multiple junctions, *SIAM J. Appl. Math.* 60 (1) (1999) 295–315, doi: [10.1137/S0036139998334895](https://doi.org/10.1137/S0036139998334895).
- [18] D.L. Olmsted, E.A. Holm, S.M. Foiles, Survey of computed grain boundary properties in face-centered cubic metals - II: Grain boundary mobility, *Acta Materialia* 57 (13) (2009) 3704–3713, doi: [10.1016/j.actamat.2009.04.015](https://doi.org/10.1016/j.actamat.2009.04.015).
- [19] K.G. Janssens, D. Olmsted, E.A. Holm, S.M. Foiles, S.J. Plimpton, P.M. Derlet, Computing the mobility of grain boundaries, *Nat. Mater.* 5 (2) (2006) 124, doi: [10.1038/nmat1559](https://doi.org/10.1038/nmat1559).
- [20] E.A. Holm, S.M. Foiles, How grain growth stops: A mechanism for grain-growth stagnation in pure materials, *Science* 328 (5982) (2010) 1138–1141, doi: [10.1126/science.1187833](https://doi.org/10.1126/science.1187833).
- [21] J.W. Cahn, Y. Mishin, A. Suzuki, Coupling grain boundary motion to shear deformation, *Acta Materialia* 54 (19) (2006) 4953–4975, doi: [10.1016/j.actamat.2006.08.004](https://doi.org/10.1016/j.actamat.2006.08.004).
- [22] H. Khater, A. Serra, R. Pond, J. Hirth, The disconnection mechanism of coupled migration and shear at grain boundaries, *Acta Materialia* 60 (5) (2012) 2007–2020, doi: [10.1016/j.actamat.2012.01.001](https://doi.org/10.1016/j.actamat.2012.01.001).
- [23] N. Combe, F. Momprou, M. Legros, Heterogeneous disconnection nucleation mechanisms during grain boundary migration, *Phys. Rev. Mater.* 3 (6) (2019) 60601, doi: [10.1103/PhysRevMaterials.3.060601](https://doi.org/10.1103/PhysRevMaterials.3.060601).
- [24] J. Han, S.L. Thomas, D.J. Srolovitz, Grain-boundary kinetics: a unified approach, *Progr. Mater. Sci.* 98 (2018) 386–476, doi: [10.1016/j.pmatsci.2018.05.004](https://doi.org/10.1016/j.pmatsci.2018.05.004).
- [25] H.F. Poulsen, *Three-Dimensional X-ray Diffraction Microscopy: Mapping Polycrystals and Their Dynamics*, 205, Springer Science & Business Media, 2004.
- [26] W. Ludwig, S. Schmidt, E.M. Lauridsen, H.F. Poulsen, X-ray diffraction contrast tomography: a novel technique for three-dimensional grain mapping of polycrystals. I. direct beam case, *J. Appl. Crystallogr.* 41 (2) (2008) 302–309, doi: [10.1107/S0021889808001684](https://doi.org/10.1107/S0021889808001684).
- [27] G. Johnson, A. King, M.G. Honnicke, J. Marrow, W. Ludwig, X-ray diffraction contrast tomography: a novel technique for three-dimensional grain mapping of polycrystals. II. the combined case, *J. Appl. Crystallogr.* 41 (2) (2008) 310–318, doi: [10.1107/S0021889808001726](https://doi.org/10.1107/S0021889808001726).
- [28] S. Schmidt, U.L. Olsen, H.F. Poulsen, H.O. Sørensen, E.M. Lauridsen, L. Margulies, C. Maurice, D.J. Jensen, Direct observation of 3-D grain growth in Al–0.1% Mn, *Scripta Materialia* 59 (5) (2008) 491–494, doi: [10.1016/j.scriptamat.2008.04.049](https://doi.org/10.1016/j.scriptamat.2008.04.049).
- [29] S.F.F. Li, *Imaging of orientation and geometry in microstructures: development and applications of high energy x-ray diffraction microscopy*, Carnegie Mellon University, 2011 Ph.D. thesis.
- [30] Y.-F. Shen, S. Maddali, D. Menasche, A. Bhattacharya, G. Rohrer, R. Suter, Importance of outliers: a three-dimensional study of coarsening in  $\alpha$ -phase iron, *Phys. Rev. Mater.* 3 (6) (2019) 63611, doi: [10.1103/PhysRevMaterials.3.063611](https://doi.org/10.1103/PhysRevMaterials.3.063611).
- [31] M. Syha, *Microstructure evolution in strontium titanate Investigated by means of grain growth simulations and x-ray diffraction contrast tomography experiments*, Karlsruhe Institute of Technology, 2014 Ph.D. thesis.
- [32] A. Trenkle, M. Syha, W. Rheinheimer, P.G. Callahan, L. Nhuyen, W. Ludwig, W.C. Lenthe, M. Echlin, T. Pollock, D. Weygand, M. De Graef, M. Hoffmann, P. Gumbsch, Non-destructive evaluation of 3D microstructure evolution in strontium titanate, *J. Appl. Crystallogr.* (2020), doi: [10.1107/S160057672000093X](https://doi.org/10.1107/S160057672000093X).
- [33] J. Sun, A. Lyckegaard, Y. Zhang, S. Catherine, B. Patterson, F. Bachmann, N. Gueninchaui, H. Bale, C. Holzner, E. Lauridsen, et al., 4D study of grain growth in Armco iron using laboratory x-ray diffraction contrast tomography, *IOP Conference Series: Materials Science and Engineering*, 219, IOP Publishing, 2017, p. 012039.
- [34] A. King, P. Reischig, J. Adrien, W. Ludwig, First laboratory x-ray diffraction contrast tomography for grain mapping of polycrystals, *J. Appl. Crystallogr.* 46 (6) (2013) 1734–1740, doi: [10.1107/S0021889813022553](https://doi.org/10.1107/S0021889813022553).
- [35] S. McDonald, P. Reischig, C. Holzner, E. Lauridsen, P. Withers, A. Merkle, M. Feser, Non-destructive mapping of grain orientations in 3D by laboratory x-ray microscopy, *Sci. Rep.* 5 (2015) 14665, doi: [10.1038/srep14665](https://doi.org/10.1038/srep14665).
- [36] J. Zhang, S.O. Poulsen, J.W. Gibbs, P.W. Voorhees, H.F. Poulsen, Determining material parameters using phase-field simulations and experiments, *Acta Materialia* 129 (2017) 229–238, doi: [10.1016/j.actamat.2017.02.056](https://doi.org/10.1016/j.actamat.2017.02.056).
- [37] J. Zhang, Y. Zhang, W. Ludwig, D. Rowenhorst, P.W. Voorhees, H.F. Poulsen, Three-dimensional grain growth in pure iron, part I. statistics on the grain level, *Acta Materialia* 156 (2018) 76–85, doi: [10.1016/j.actamat.2018.06.021](https://doi.org/10.1016/j.actamat.2018.06.021).
- [38] W. Ludwig, P. Reischig, A. King, M. Herbig, E. Lauridsen, G. Johnson, T. Marrow, J.-Y. Buffiere, Three-dimensional grain mapping by x-ray diffraction contrast tomography and the use of Friedel pairs in diffraction data analysis, *Rev. Sci. Instrum.* 80 (3) (2009) 33905, doi: [10.1063/1.3100200](https://doi.org/10.1063/1.3100200).
- [39] P. Reischig, A. King, L. Nervo, N. Viganó, Y. Guilhem, W.J. Palenstijn, K. Batenburg, M. Preuss, W. Ludwig, Advances in x-ray diffraction contrast tomography: flexibility in the setup geometry and application to multiphase materials, *J. Appl. Crystallogr.* 46 (2) (2013) 297–311, doi: [10.1107/S0021889813002604](https://doi.org/10.1107/S0021889813002604).
- [40] G.B. Vaughan, J.P. Wright, A. Bytchkov, M. Rossat, H. Gleyzolle, I. Snigireva, A. Snigirev, X-ray transfectors: focusing devices based on compound refractive lenses, *J. Synchrotron Radiat.* 18 (2) (2011) 125–133, doi: [10.1107/S0909049510044365](https://doi.org/10.1107/S0909049510044365).
- [41] I. McKenna, M. Gururajan, P.W. Voorhees, Phase field modeling of grain growth: effect of boundary thickness, triple junctions, misorientation, and anisotropy, *J. Mater. Sci.* 44 (9) (2009) 2206–2217, doi: [10.1007/s10853-008-3196-7](https://doi.org/10.1007/s10853-008-3196-7).
- [42] T. Takaki, T. Hirouchi, Y. Hisakuni, A. Yamanaka, Y. Tomita, Multi-phase-field model to simulate microstructure evolutions during dynamic recrystallization, *Mater. Trans.* 49 (11) (2008) 2559–2565, doi: [10.2320/matertrans.MB200805](https://doi.org/10.2320/matertrans.MB200805).
- [43] A. Yamanaka, T. Takaki, T. Aoki, T. Shimokawabe, Multiphase field simulation of austenite-to-ferrite transformation accelerated by GPU computing, *J. Comput. Sci. Technol.* 6 (3) (2012) 182–197, doi: [10.1299/jcst.6.182](https://doi.org/10.1299/jcst.6.182).
- [44] J. Zhang, *Determination of material parameters by comparison of 3D simulations and 3D experiments*, Technical University of Denmark, 2018 Ph.D. thesis.
- [45] B.R. Patterson, D.J. Rule, R. DeHoff, V. Tikare, Schlegel description of grain form evolution in grain growth, *Acta Materialia* 61 (11) (2013) 3986–4000, doi: [10.1016/j.actamat.2013.03.013](https://doi.org/10.1016/j.actamat.2013.03.013).

- [46] G. Gottstein, L. Shvindlerman, B. Zhao, Thermodynamics and kinetics of grain boundary triple junctions in metals: recent developments, *Scripta Materialia* 62 (12) (2010) 914–917, doi: [10.1016/j.scriptamat.2010.03.017](https://doi.org/10.1016/j.scriptamat.2010.03.017).
- [47] A.E. Johnson, P.W. Voorhees, A phase-field model for grain growth with trijunction drag, *Acta Materialia* 67 (2014) 134–144, doi: [10.1016/j.actamat.2013.12.012](https://doi.org/10.1016/j.actamat.2013.12.012).
- [48] J. Hamilton, D.J. Siegel, I. Daruka, F. Léonard, Why do grain boundaries exhibit finite facet lengths? *Phys. Rev. Lett.* 90 (24) (2003) 246102, doi: [10.1103/PhysRevLett.90.246102](https://doi.org/10.1103/PhysRevLett.90.246102).
- [49] S. Ahl, H. Simons, Y. Zhang, C. Detlefs, F. Støhr, A. Jakobsen, D.J. Jensen, H. Poulsen, Ultra-low-angle boundary networks within recrystallizing grains, *Scripta Materialia* 139 (2017) 87–91, doi: [10.1016/j.scriptamat.2017.06.016](https://doi.org/10.1016/j.scriptamat.2017.06.016).
- [50] Y. Zhang, T. Andriollo, S. Fæster, R. Barabash, R. Xu, N. Tiedje, J. Thorborg, J. Hattel, D.J. Jensen, N. Hansen, Microstructure and residual elastic strain at graphite nodules in ductile cast iron analyzed by synchrotron x-ray microdiffraction, *Acta Materialia* 167 (2019) 221–230, doi: [10.1016/j.actamat.2019.01.038](https://doi.org/10.1016/j.actamat.2019.01.038).
- [51] H. Simons, A. King, W. Ludwig, C. Detlefs, W. Pantleon, S. Schmidt, F. Støhr, I. Snigireva, A. Snigirev, H.F. Poulsen, Dark-field x-ray microscopy for multiscale structural characterization, *Nat. Commun.* 6 (2015) 6098, doi: [10.1038/ncomms7098](https://doi.org/10.1038/ncomms7098).
- [52] Y. Zhang, J. Budai, J.Z. Tischler, W. Liu, R. Xu, E. Homer, A. Godfrey, D.J. Jensen, Boundary migration in a 3D deformed microstructure inside an opaque sample, *Sci. Rep.* 7 (1) (2017) 4423, doi: [10.1038/s41598-017-04087-9](https://doi.org/10.1038/s41598-017-04087-9).
- [53] A. Jakobsen, H. Simons, W. Ludwig, C. Yildirim, H. Leemreize, L. Porz, C. Detlefs, H. Poulsen, Mapping of individual dislocations with dark-field x-ray microscopy, *J. Appl. Crystallogr.* 52 (1) (2019) 122–132, doi: [10.1107/S1600576718017302](https://doi.org/10.1107/S1600576718017302).
- [54] K.T. Murray, A.F. Pedersen, I. Mohacsi, C. Detlefs, A.J. Morgan, M. Prasciolu, C. Yildirim, H. Simons, A.C. Jakobsen, H.N. Chapman, et al., Multilayer Laue lenses at high x-ray energies: performance and applications, *Opt. Express* 27 (5) (2019) 7120–7138, doi: [10.1364/OE.27.007120](https://doi.org/10.1364/OE.27.007120).
- [55] G.B. Olson, Computational design of hierarchically structured materials, *Science* 277 (5330) (1997) 1237–1242, doi: [10.1126/science.277.5330.1237](https://doi.org/10.1126/science.277.5330.1237).